


Type-II antiferromagnetic ordering in the double perovskite oxide Sr₂NiWO₆Cheng Su,^{1,*} Xu-Tao Zeng^{1,*} Kaitong Sun^{2,*} Denis Sheptyakov,³ Ziyu Chen,¹
Xian-Lei Sheng¹ Haifeng Li^{2,†} and Wentao Jin^{1,‡}¹*School of Physics, Beihang University, Beijing 100191, China*²*Joint Key Laboratory of the Ministry of Education, Institute of Applied Physics and Materials Engineering, University of Macau, Avenida da Universidade, Taipa, Macao SAR 999078, China*³*Laboratory for Neutron Scattering and Imaging, Paul Scherrer Institut, CH-5232 Villigen-PSI, Switzerland* (Received 27 February 2023; revised 20 June 2023; accepted 24 July 2023; published 10 August 2023)

Magnetic double perovskite (DP) compounds provide a fertile playground to explore interesting electronic and magnetic properties. By complementary macroscopic characterizations, neutron powder diffraction measurements, and first-principles calculations, we have performed comprehensive studies on the magnetic ordering in the DP compound Sr₂NiWO₆. It is found by neutron diffraction to order magnetically in a collinear type-II antiferromagnetic (AFM) structure in a tetragonal lattice with $k = (0.5, 0, 0.5)$ below $T_N = 56$ K. In the ground state, the ordered moment of the spin-1 Ni²⁺ ions is determined to be 1.9(2) μ_B , indicating a significant quenching of the orbital moment. The Ni²⁺ moments in Sr₂NiWO₆ are revealed to cant off the c axis by 29.2°, which is well supported by the first-principles magnetic anisotropy energy calculations. Furthermore, the in-plane and out-of-plane next-nearest-neighbor superexchange couplings (J_2 and J_{2c}) are found to play a dominant role in the spin Hamiltonian of Sr₂NiWO₆, which accounts for the stabilization of the type-II AFM structure as its magnetic ground state.

DOI: [10.1103/PhysRevB.108.054416](https://doi.org/10.1103/PhysRevB.108.054416)**I. INTRODUCTION**

Perovskite oxide ABO_3 has drawn great attention and interest during the past few decades [1,2], owing to its highly tunable physical properties and promising applications in electronic or spintronic devices [3,4], fuel cells [5], solar cells [6], and so on, arising from its highly flexible chemical and structural properties. As a variant of the perovskite structure, the B -site ordered double-perovskite (DP) oxides with the general formula of $A_2BB'O_6$ (A being a divalent or trivalent metal, B and B' being transition-metal ions alternately arranged in a rock-salt structure and surrounded by corner-sharing oxygen octahedra) have been the focus of intensive studies in recent years [7,8] because of various intriguing electronic and magnetic properties that may be realized in this large family. The most well-known example is Sr₂FeMoO₆ with a high Curie temperature of $T_C \sim 420$ K and a large room-temperature magnetoresistance, as a result of the strong $3d$ - $4d$ hybridization between the Fe³⁺ and Mo⁵⁺ ions [9,10]. Such a hybridization between the B and B' ions is also evidenced in $3d$ - $5d$ DP rhenates and iridates [11–14], in which the strong spin-orbit coupling (SOC) on $5d$ ions may give rise to anisotropic and bond-dependent magnetic interactions.

For magnetic B -site ions located in the center of the BO_6 octahedra, although the direct exchange interaction is negligible due to the large distance between them, the

nearest-neighbor (NN) and next-NN (NNN) superexchange interactions can take place over 90° B -O-(B')-O- B and 180° B -O- B' -O- B paths, respectively. Typically, the B -site ordered DP with a single magnetic sublattice shows low-temperature antiferromagnetic (AFM) ordering. Depending on the identities of B and B' ions and the relative strength of NN (J_1) and NNN (J_2) interactions, different types of AFM structures have been observed [15–17]. As two distinct examples, the magnetic ground state of Sr₂CuTeO₆ is Néel-type AFM ordering, as expected for $J_2 < J_1$ [18], while Sr₂CuWO₆ exhibits type-II AFM ordering, as expected for $J_2 > J_1$ [19]. Accordingly, they show quasi-two-dimensional (2D) and three-dimensional (3D) natures, respectively, associated with the magnetism of the $S = \frac{1}{2}$ Cu²⁺ ions.

Sr₂NiWO₆ (SNWO) is a B -site ordered DP oxide, whose detailed magnetic structure of $S = 1$ Ni²⁺ moments is unknown so far. The divalent magnetic Ni²⁺ ions and hexavalent diamagnetic W⁶⁺ ions occupy the B and B' sites, respectively, forming interpenetrating face-centered cubic (FCC) lattices. It crystallizes in a tetragonal structure (space group $I4/m$) at the ambient condition [20–22] and undergoes a tetragonal-to-cubic structural phase transition above 300 °C [23,24]. Interestingly, SNWO was found to order antiferromagnetically at a rather high Néel temperature of $T_N = 54$ – 59 K [20–22,25], despite a very long superexchange path (Ni-O-W-O-Ni) of ~ 8 Å. Although an *ab initio* calculation predicts the type-II AFM ordering (AFM-II structure) as its magnetic ground state [26], which is consistent with the expectation from the inelastic neutron scattering measurements [25], and on the other hand, a similar DP oxide Ba₂NiWO₆ was proved to be of a type-II AFM structure as well [27],

*These authors contributed equally to this work.

†haifengli@um.edu.mo

‡wtjin@buaa.edu.cn

direct confirmation using magnetic neutron diffraction and detailed knowledge of the moment size and direction in SNWO are still lacking, which impedes a thorough understanding about the spin interactions and the origin of AFM ordering in SNWO.

In this paper, we have conducted comprehensive studies on the magnetic ordering in SNWO, combining macroscopic and microscopic experimental probes and first-principles calculations. Using neutron diffraction as the microscopic probe, we have provided solid evidence that SNWO orders magnetically in a type-II AFM structure with $k = (0.5, 0, 0.5)$ below $T_N = 56$ K, in good agreement with the previous theoretical prediction. At the base temperature, the Ni^{2+} moments in SNWO are found to cant off the c axis by 29.2° , well supported by the first-principles magnetic anisotropy energy (MAE) calculations. The strengths of the superexchange couplings are also estimated to understand the origin of the experimentally determined type-II AFM structure.

II. METHODS

Polycrystalline samples of Sr_2NiWO_6 were synthesized by a standard solid-state reaction method, as reported in Ref. [22]. NiWO_4 , the precursor material, was firstly synthesized by sintering a stoichiometric mixture of WO_3 (99.99%) and NiO (99.9%) in air, at 1000°C for 10 h. Then the synthesized NiWO_4 powder was mixed with SrCO_3 (99.95%) with a stoichiometric ratio of 1:2 and sintered in air at 1400°C for 8 h. The powder mixture in each procedure mentioned above needs to be thoroughly ground and pelletized before sintering. The phase purity was checked by a room-temperature x-ray diffraction (XRD) measurement on a Bruker D8 ADVANCE diffractometer with $\text{Cu-K}\alpha$ radiation ($\lambda = 1.5406 \text{ \AA}$).

The neutron powder diffraction (NPD) experiments were carried out on the High Resolution Powder diffractometer for Thermal neutrons (HRPT) [28] at the Swiss Neutron Spallation Source (SINQ), at the Paul Scherrer Institute in Villigen, Switzerland. A powder sample of SNWO with a total mass of 5.5 g was loaded into a 8-mm-diameter vanadium can. The diffraction patterns were collected using wavelengths $\lambda = 1.1545, 1.494, \text{ and } 2.45 \text{ \AA}$ in the temperature range from 1.5 to 300 K. The shorter wavelengths cover a wider Q range suitable for refining the structural parameters, while the longer wavelength provides a higher resolution in the lower Q range for a more reliable determination of magnetic structure. Refinements of the nuclear and magnetic structures were conducted using the FULLPROF program suite [29].

First-principles calculations were performed on the basis of density functional theory (DFT) using the generalized gradient approximation (GGA) in the form proposed by Perdew *et al.* [30], as implemented in VASP [31,32]. The energy cutoff of the plane wave was set to 500 eV. The energy convergence criterion in the self-consistent calculations was set to 10^{-6} eV. A Γ -centered Monkhorst-Pack k -point mesh with a resolution of $2\pi \times 0.03 \text{ \AA}^{-1}$ was used for the first Brillouin zone sampling. To account for the correlation effects for Ni, we adopted the GGA + U method [33] with the value of $U = 5$ eV, which is commonly used in studying nickel compounds [34].

III. RESULTS AND DISCUSSIONS

A. Structural characterizations

Figures 1(a) and 1(b) show the room-temperature XRD and NPD patterns of the synthesized polycrystalline SNWO sample, respectively, which can be well fitted using the reported tetragonal phase of SNWO [21–23] with satisfactory R factors. Tiny amounts of impurity phases were detected in x-ray (SrWO_4 , 0.9 wt. %) and neutron (NiO , 0.5 wt. %) powder diffraction data and included in the corresponding Rietveld refinements. The contribution of SrWO_4 to the neutron powder data was, however, so weak that it could be omitted in the refinements.

Due to the relatively large coherent neutron scattering length of oxygen atoms, the room-temperature structural parameters of SNWO including all atomic coordinates can be precisely determined by Rietveld refinements to the NPD pattern shown in Fig. 1(b) and listed in Table I. According to our refinements, the atomic coordinates are consistent with those reported [21,23,35], and no obvious site mixing between Ni and W was observed. Thus, the actual structure of the synthesized SNWO is indeed a rock-salt-type B -site ordered DP [see Fig. 1(c)].

As illustrated in Fig. 1(d), the adjacent NiO_6 and WO_6 octahedra display out-of-phase rotations around the c axis (denoted as an $a^0a^0c^-$ rotation pattern in the well-adopted Glazer notation in describing the perovskite structures [36]), yielding an in-plane Ni-O(1)-W bond angle of 167.55° and a tetragonal symmetry at 300 K, in contrast to a non-distorted 180° Ni-O(1)-W bond angle associated with the cubic symmetry at very high temperature [23,24]. Such a lattice distortion has been widely reported in various DP compounds [7], which releases the stress caused by the mismatch of ionic radius on the B and B' sites and thus provides great tolerance of the DP structure to accommodate most elements in the periodic table.

B. Macroscopic magnetic properties

The temperature dependence of the DC magnetic susceptibility of the polycrystalline SNWO measured in an applied magnetic field of 1 T is shown in Fig. 2(a), which clearly indicates a typical AFM transition at $T_N = 56(1)$ K, consistent with the previously reported Néel temperature of 54–59 K [20–22,25]. By performing a Curie-Weiss fitting to the inverse magnetic susceptibility ($1/\chi$) in the paramagnetic state from 200 to 300 K, an effective magnetic moment of $\mu_{\text{eff}} = 3.127(2) \mu_B$ for the Ni^{2+} ions and a Curie-Weiss temperature of $\theta = -92.8(3)$ K are obtained. The μ_{eff} value is close to the spin-only moment value of $2.83 \mu_B$ for the spin-1 Ni^{2+} ions, suggesting the significant quenching of their orbital angular momentum in the octahedral coordination formed by surrounding oxygen ions.

The large negative value of $\theta \sim -10^2$ K suggests a very strong dominant AFM interaction between the Ni^{2+} moments in SNWO, which is further supported by the isothermal magnetization curve measured at 4 K, as shown in the inset of Fig. 2(a). Up to 14 T, the measured magnetization is still far below the saturated value of $\mu_S = 2 \mu_B$ per Ni^{2+} ion with the spin-only moment (assuming Landé factor $g = 2$), as a free spin-1 ion coupling with a 14 T magnetic field is estimated to

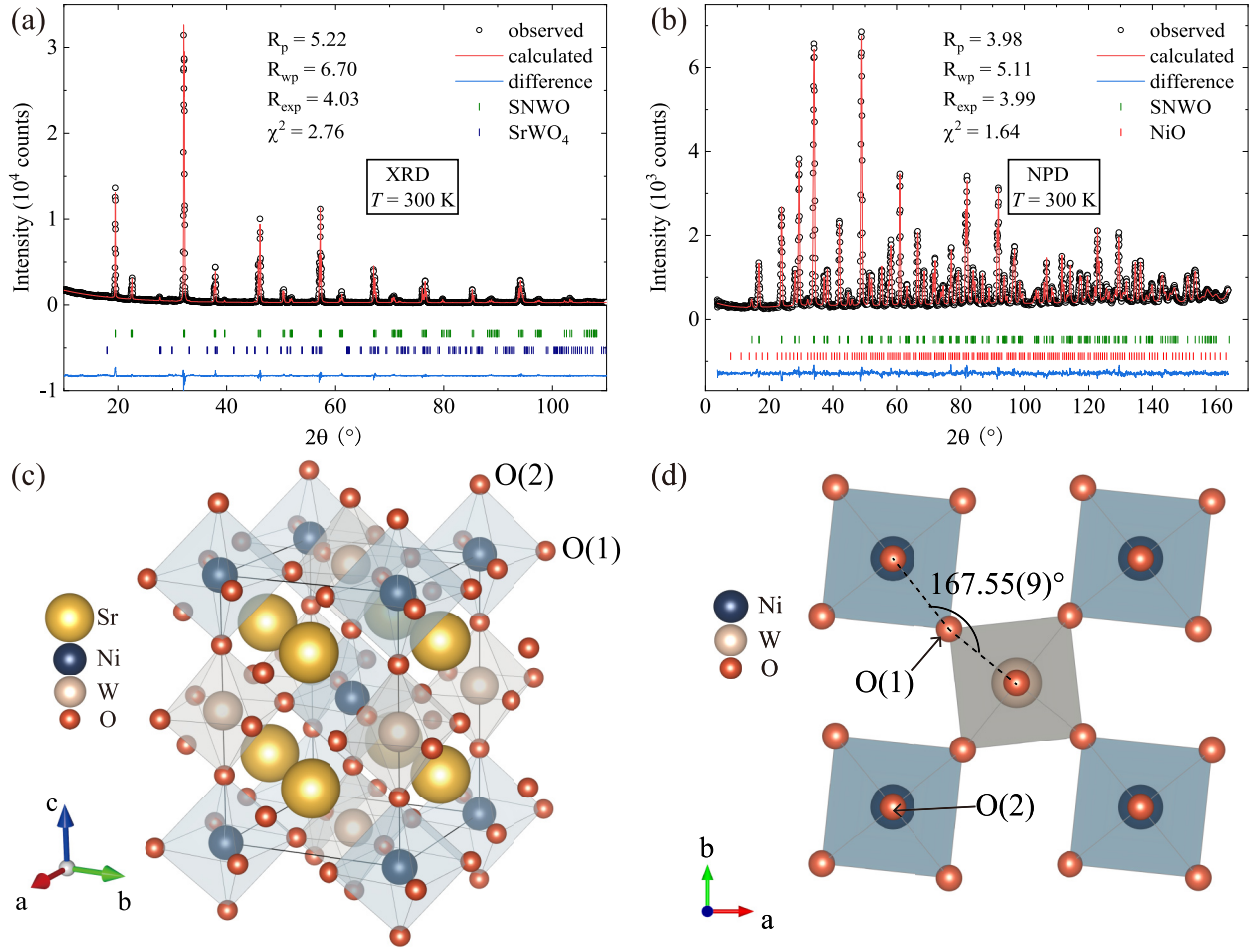


FIG. 1. Room-temperature (a) x-ray diffraction (XRD) and (b) neutron powder diffraction (NPD) patterns of the polycrystalline SNWO sample and (c) and (d) the corresponding crystal structures. In (a) and (b), the black circles represent the observed intensities, and the red solid line is the calculated pattern according to the Rietveld refinement. The difference between the observed and calculated intensities is shown as the blue line at the bottom. The olive, red, and navy vertical bars indicate the Bragg reflections from the SNWO main phase, NiO, and SrWO₄ impurities, respectively. (d) illustrates the projection of the lattice of SNWO onto the *ab* plane, showing the out-of-phase rotations of NiO₆ and WO₆ octahedra along the *c* axis and the resultant in-plane Ni-O(1)-W bond angle of 167.55° at 300 K.

obtain an Zeeman energy of ~ 20 K, which is far below the characteristic temperature of $\theta = -92.8(3)$ K.

TABLE I. Refinement results of the lattice parameters, atomic coordinates, and thermal factors of SNWO at 300 and 1.5 K, respectively (space group $I4/m$, $Z = 2$).

Atom (site)	<i>x</i>	<i>y</i>	<i>z</i>	$B_{\text{iso}}(\text{Å}^2)$
$T = 300$ K	$a = b = 5.5598(1)\text{Å}$,		$c = 7.9173(2)\text{Å}$	
O(1) ($8h$)	0.2843(3)	0.2298(3)	0	0.79(2)
O(2) ($4e$)	0	0	0.2566(4)	0.87(2)
W ($2b$)	0	0	0.5	0.57(4)
Sr ($4d$)	0	0.5	0.25	0.60(1)
Ni ($2a$)	0	0	0	0.20(2)
$T = 1.5$ K	$a = b = 5.5409(2)\text{Å}$,		$c = 7.9264(2)\text{Å}$	
O(1) ($8h$)	0.2912(3)	0.2246(3)	0	0.38(2)
O(2) ($4e$)	0	0	0.2576(4)	0.33(3)
W ($2b$)	0	0	0.5	0.42(6)
Sr ($4d$)	0	0.5	0.25	0.17(2)
Ni ($2a$)	0	0	0	0.05(3)

In addition, as shown in Fig. 2(b), the molar specific heat (C) of SNWO also shows a clear anomaly at ~ 54 K, supporting the long-range nature of the AFM ordering revealed in Fig. 2(a). It is worth noting that such an anomaly around T_N is hardly affected by the external field up to 14 T, further corroborating the robustness of the AFM interactions in SNWO against the external perturbation. To further obtain the magnetic specific heat of SNWO, two different approaches are adopted to estimate the phonon contribution. The first method is to approximate the phonon specific heat by the Debye model. A two-component model assuming two different Debye temperatures:

$$C_{\text{ph}} = 9R \sum_{i=1}^2 c_i \left(\frac{T}{\theta_{D_i}} \right)^3 \int_0^{\theta_{D_i}/T} dx \frac{x^4 e^x}{(e^x - 1)^2},$$

is used with the constrain of $c_1 + c_2 = 10$, as there are 10 atoms in total in one chemical formula unit. The best fit converges to values of $c_1 = 5.607$, $c_2 = 4.393$, $\theta_{D1} = 293.5$ K, and $\theta_{D2} = 868.5$ K. Considering the large atomic mass difference in SNWO (for example, W and O atoms),

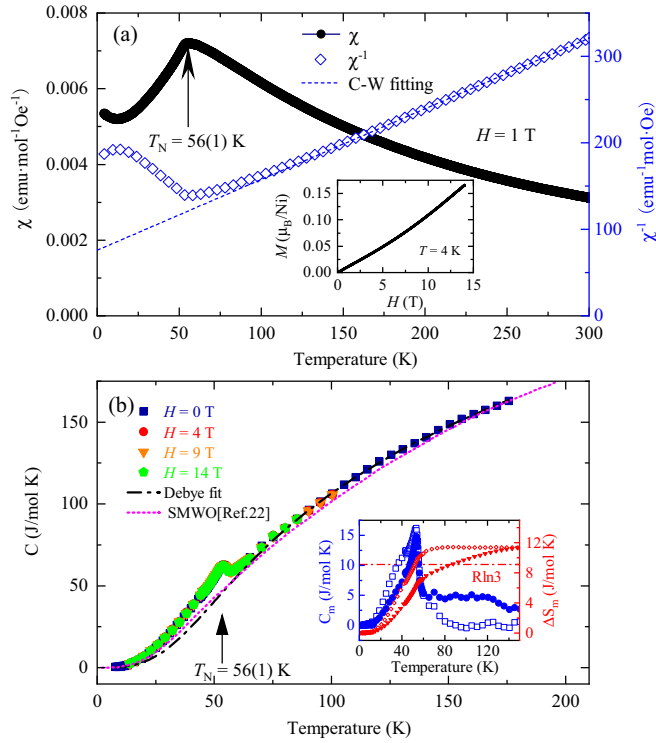


FIG. 2. (a) DC magnetic susceptibility (χ , black circles) and inverse susceptibility ($1/\chi$, blue squares) of the polycrystalline SNWO sample, measured in a magnetic field of 1 T. The dashed line represents the Curie-Weiss fitting to $1/\chi$ from 200 to 300 K. The inset shows the isothermal magnetization curve measured at 4 K. (b) Molar specific heat C of SNWO measured in the magnetic field of 0, 4, 9, and 14 T, respectively. The dashed line represents a fitting to the phonon contribution C_{ph} to the zero-field specific heat. The black dashed line represents the two-component Debye model fitting, and the magenta dotted line represents the specific heat of polycrystalline Sr_2MgWO_6 extracted from Ref. [22]. The inset shows the magnetic specific heat C_m (blue squares from the former approach and circles from the latter) after the phonon subtraction and the change of magnetic entropy ΔS_m (red diamonds from the former approach and triangles from the latter) calculated by integrating C_m/T . For comparison, the expected ΔS_m value of $R\ln 3$ is also marked.

this two-component model can be interpreted as the division of atoms into the light and heavy groups, as widely adopted in many other materials [37–39]. With this estimated phonon specific heat subtracted, the magnetic specific heat (C_m) is obtained, and the corresponding magnetic entropy change (ΔS_m) is calculated by integrating C_m/T over the temperature, as shown by the open squares and diamonds in the inset of Fig. 2(b), respectively. The other method to subtract the phonon specific heat is to use a nonmagnetic analog. Here, we refer to the experimental data of polycrystalline Sr_2MgWO_6 (SMWO) from Ref. [22]. By multiplying a factor of 1.106 to the specific heat of SMWO to have its high-temperature behavior overlapped with that of our SNWO, the magnetic specific heat of SNWO can be obtained as well after the subtraction, and ΔS_m is calculated accordingly, as shown by the solid circles and triangles in the inset of Fig. 2(b). Using either of the two approaches presented above, the experimental maximal change of magnetic entropy ΔS_m

is estimated to be $\sim 11.5 \text{ J K}^{-1} \text{ mol}^{-1}$ up to 150 K. Considering the approximation in the Debye model of taking phonon density of states as quadratic forms and the substantial difference between the atomic mass of Mg and Ni in SMWO and SNWO, both approaches cannot capture the phonon behaviors precisely. Therefore, the difference between the measured magnetic entropy change and the theoretically expected value for a spin-1 system [$\Delta S_m = R\ln(2S+1) = R\ln 3 = 9.134 \text{ J K}^{-1} \text{ mol}^{-1}$] can be due to an imprecise estimation of the phonon contributions. However, the characterization about the specific heat still clearly suggests that the magnetism of Ni^{2+} spins can be well described by $S = 1$.

C. Magnetic structure determination

Low-temperature NPD measurements were carried out to determine the magnetic structure of SNWO below the AFM transition at T_N . Figure 3 shows the NPD patterns collected at (a) and (b) 100 K and (c) and (d) 1.5 K using the wavelengths of 1.1545 and 2.45 Å and the results of the Rietveld refinements accordingly. At 100 K, well above T_N , the diffraction patterns can be perfectly fitted by the same tetragonal phase of SNWO as the room temperature [see Figs. 3(a) and 3(b)]. Upon cooling, as shown in Figs. 3(c) and 3(d), for the base temperature of 1.5 K, additional reflections arising from the AFM ordering of Ni^{2+} moments marked by the navy vertical bars emerge, which can be well indexed with a magnetic propagation vector $k = (0.5, 0, 0.5)$.

To deduce the ground-state magnetic structure of SNWO, an irreducible representation analysis was performed first using the BASIREPS program integrated into the FULLPROF suite. For Ni^{2+} ions locating at the $2a$ Wyckoff position of the tetragonal lattice with the $I4/m$ space group, only one irreducible representation (IR) Γ_1 is possible for $k = (0.5, 0, 0.5)$ whose basis vectors are listed in Table II. The three basis vectors (ψ_ν , real unit vectors along three crystallographic axes) suggest the possibility of pointing to any direction for the Ni^{2+} moments.

With the combination of the magnetic basis vectors, the additional magnetic reflections emerging below T_N can be fitted to determine the size and direction of the Ni^{2+} moments. By simultaneous refinements to the 1.1545 and 2.45 Å datasets shown in Figs. 3(c) and 3(d), both the nuclear and magnetic structures of SNWO at the base temperature of 1.5 K can be determined with satisfactory R factors. The crystallographic parameters at 1.5 K from the nuclear structure refinement are also listed in Table I to compare with those at 300 K. At the base temperature, SNWO shows an overall similar tetragonal structure but an even larger octahedral rotation with the in-plane Ni-O(1)-W bond angle of 164.81° compared with 167.55° at 300 K.

According to the refined coefficients of the three basis vectors of the IR Γ_1 , the Ni^{2+} magnetic moment in SNWO is determined to be $1.9(2)\mu_B$ in size at 1.5 K, with components of $-0.65(16)$, $0.69(29)$, and $1.70(11)\mu_B$ along the crystallographic a , b , and c axes, respectively. Such a moment value is consistent with that expected for the spin-only $S = 1 \text{ Ni}^{2+}$ moments showing an ordered moment value of $gS = 2\mu_B$, adopting the Landé factor $g = 2$ for spin-only cases. It is also in good agreement with the observed moment

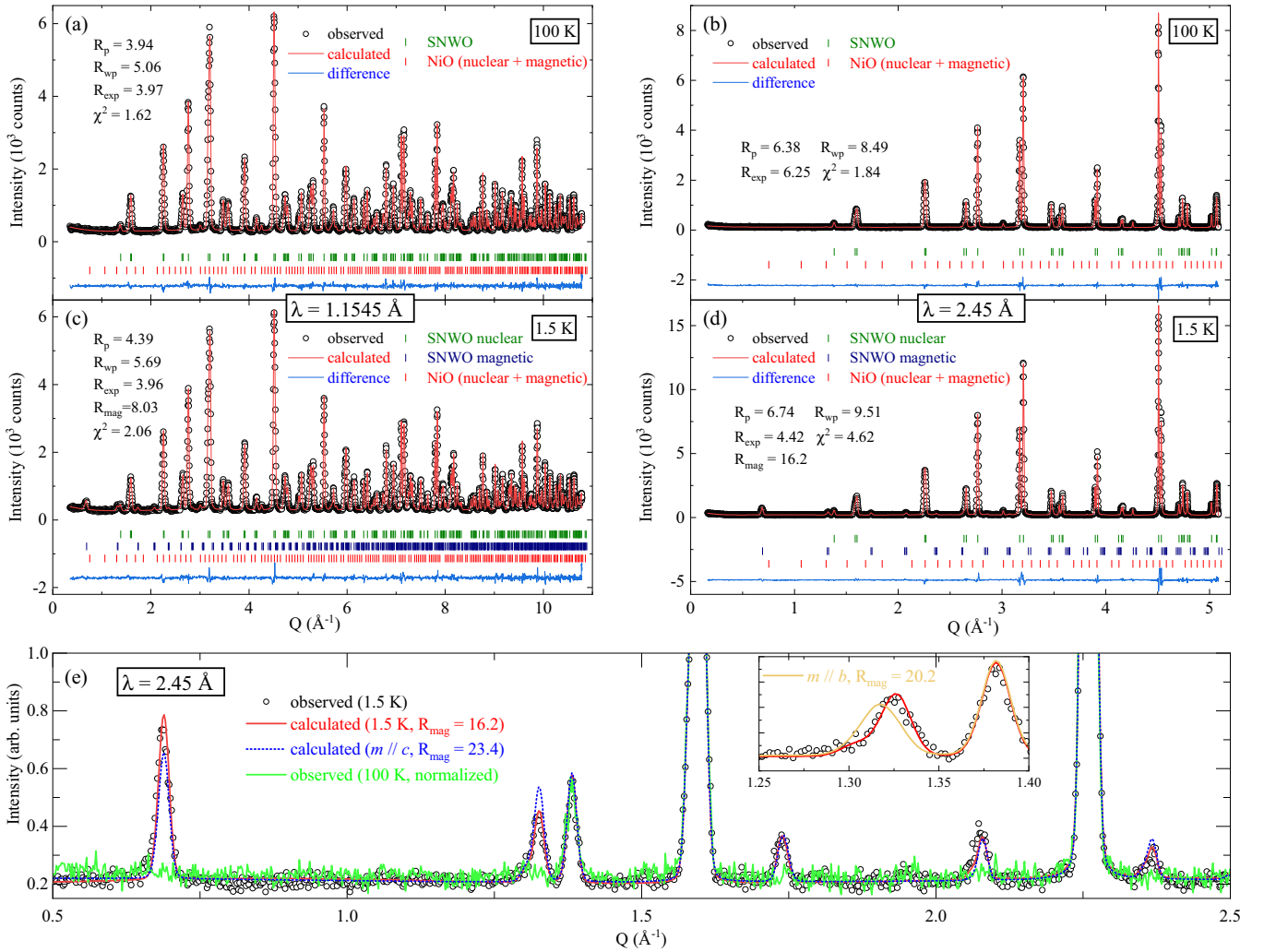


FIG. 3. Neutron powder diffraction (NPD) patterns of SNWO at (a) and (b) 100 K and (c) and (d) 1.5 K and the corresponding Rietveld refinements. The left (a) and (c) and right (b) and (d) panels show the data collected with the neutron wavelengths of 1.1545 and 2.45 Å, respectively. The Rietveld refinements at 1.5 K were performed adopting the magnetic structure described in the text. The black open circles represent the observed intensities, and the calculated patterns according to the refinements are shown as red solid lines. The differences between the observed and calculated intensities are plotted at the bottom as blue solid lines. The olive, navy, and red vertical bars indicate the nuclear Bragg reflections from SNWO, magnetic reflections from SNWO, and NiO impurity (nuclear and magnetic reflections), respectively. (e) shows the low- Q NPD patterns collected using $\lambda = 2.45$ Å at 1.5 and 100 K. The refinements to the 1.5 K pattern with three different magnetic structures, by completely relaxing the direction of Ni^{2+} moments, or fixing it along the c or b axis, are plotted as red solid line, blue dotted line, and orange solid line (in the inset), respectively, for comparison. NPD pattern collected at 100 K is normalized and plotted as a green line, while the 1.5 K pattern is plotted as black open circles.

value of 1.8–2.2 μ_B in various nickel compounds with NiO_6 octahedra as determined by neutron diffraction [40–42], further supporting the significant quenching of the orbital

TABLE II. Basis vectors (ψ_ν) of Γ_1 , the only possible magnetic IR, for the Ni atoms occupying the $2a$ sites in SNWO with the space group $I4/m$ and $k = (0.5, 0, 0.5)$, obtained from representation analysis.

IR	ψ_ν	Components	Ni
Γ_1	ψ_1	Real	(1,0,0)
	ψ_2	Real	(0,1,0)
	ψ_3	Real	(0,0,1)

moment for the Ni^{2+} ions in SNWO, as evidenced by the dc magnetic susceptibility data presented in Sec. III B.

In addition, we note that, in a previous *ab initio* investigation of the magnetic ordering in SNWO, it was proposed that the AFM-II configuration with the moments aligned along the c axis is energetically favorable [26]. In Fig. 3(e), we have shown the refinements to the 2.45 Å NPD pattern collected at 1.5 K using two different magnetic structures, by completely relaxing the direction of Ni^{2+} moments or fixing it along the c axis for comparison. It is clear that the latter yields a much worse agreement with the observed intensities in the low- Q region ($R_{\text{mag}} = 23.4$) compared with the former ($R_{\text{mag}} = 16.2$). Additionally, for comparison, the inset of Fig. 3(e) displays the refinement result fixing moments along the b axis

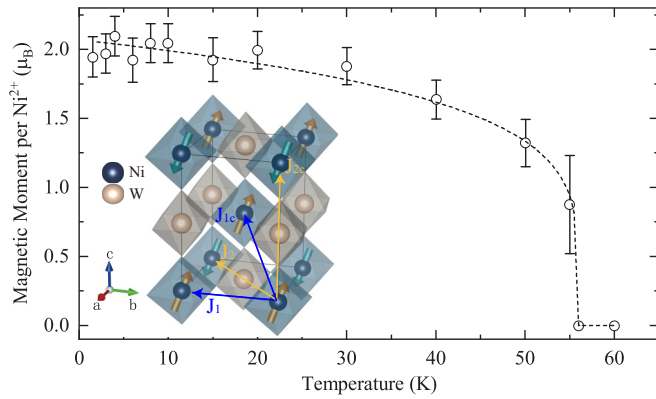


FIG. 4. Temperature dependence of the refined moment size of the Ni^{2+} ions, where the dashed line represents a power-law fitting. The inset illustrates the experimentally determined type-II antiferromagnetic (AFM) structure of SNWO in the ground state, in which the blue arrows represent the in-plane and out-of-plane nearest-neighbor (NN) exchange couplings (J_1 and J_{1c}) and the yellow arrows represent the in-plane and out-of-plane next-nearest-neighbor (NNN) exchange couplings (J_2 and J_{2c}).

($R_{\text{mag}} = 20.2$). The failure of fitting the 1.33 \AA^{-1} peak also verifies the necessity of the a/c axis component, suggesting the validity of the refined result of $\vec{m}_{\text{exp}} = (-0.65, 0.69, 1.70) \mu_{\text{B}}$ with components along all three crystallographic axes.

Figure 4 shows the refined moment size in SNWO as a function of temperature, which can be regarded as the order parameter associated with the AFM transition. As the dashed line presents, below $T_{\text{N}} = 56 \text{ K}$ (as determined in Sec. III B), the AFM order parameter follows a power-law behavior $M \propto (T_{\text{N}} - T)^{\beta}$, with the exponent β fitted to be $0.20(4)$. It is worth pointing out that the β value determined here cannot be directly compared with the universal critical exponent associated with the magnetic ordering, as Fig. 4 does not contain enough data points in the critical region close to T_{N} .

Associated with $k = (0.5, 0, 0.5)$, the ground-state magnetic structure of SNWO is depicted as the inset of Fig. 4. The Ni^{2+} spins align antiparallely along both the a and c axes, but align parallelly along the b axis, forming a type-II AFM structure. Such a type-II AFM structure was previously reported for the DP tungstates Sr_2CuWO_6 and $(\text{Ba}/\text{Sr})_2\text{FeWO}_6$, ascribed to a dominant NNN interaction J_2 in their spin Hamiltonian [19,43]. The ordering pattern of the Ni^{2+} spins is consistent with the AFM-II configuration theoretically predicted for SNWO in Ref. [26], but the moment direction differs a lot. The reason for such a discrepancy will be discussed in Sec. III D.

D. First-principles calculations

To compare with the experimentally determined magnetic structure of SNWO, the energies of 801 different spin orientations uniformly distributed in the real space have been calculated within the frame of DFT. Figure 5(a) shows the 2D angular dependence of the MAE obtained by linear interpolations to the calculated values, with respect to the magnetic ground state. By setting a Cartesian coordinate system with its x , y , and z axes overlapped with the a , b , and c axes of the tetragonal lattice, the direction of the Ni^{2+} moments can be fully described by angles θ and φ , as illustrated in the inset of Fig. 5(b). The calculated petal-like MAE pattern near the center area in Fig. 5(a) displays fourfold rotational symmetry around the central point ($\theta = 90^\circ$), suggesting C_{4z} symmetry from the perspective of DFT, which is not surprising considering the tetragonal symmetry of SNWO at low temperatures. The C_{4z} symmetry is better visualized in the φ dependence of the in-plane MAE, as shown in Fig. 5(b), with θ fixed to be 0.

According to the calculation, the spin orientation with the moment size converged to $\vec{m}_{\text{cal}} = (-0.89, 0.71, 1.65) \mu_{\text{B}}$ per formula unit shows the lowest energy, corresponding to $\theta = 55.5^\circ$ and $\varphi = 141^\circ$, as marked by the white triangle in Fig. 5(a). This calculated energy-preferred direction is highly consistent with the experimentally determined orientation of $\vec{m}_{\text{exp}} = (-0.65, 0.69, 1.70) \mu_{\text{B}}$ [corresponding to $\theta = 60.8^\circ$

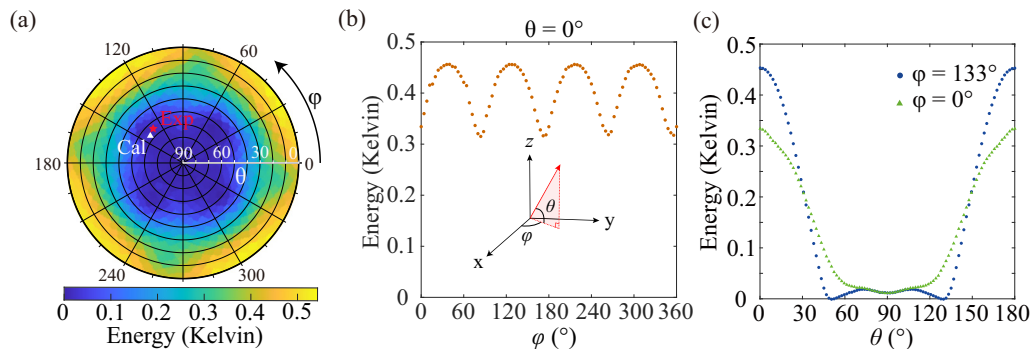


FIG. 5. Angular dependence of the calculated magnetic anisotropy energy (MAE). (a) shows the two-dimensional (2D) contour map of the MAE as functions of angles θ and φ , which are defined in the Cartesian coordinate system overlapped with the a , b , and c axes of the tetragonal lattice, as shown in the inset of (b). The color represents the relative energy of certain spin orientation calculated by density functional theory (DFT), with respect to the magnetic ground state. The moment directions found experimentally and theoretically, according to the neutron data and the minimum of the calculated MAE, are labeled by the red star and white triangle, respectively. (b) shows the φ dependence of the MAE (or in-plane MAE) with fixed $\theta = 0$. (c) shows the θ dependence of the MAE (or out-of-plane MAE) with fixing $\varphi = 133^\circ$ (the experimentally found value) and $\varphi = 0^\circ$, respectively.

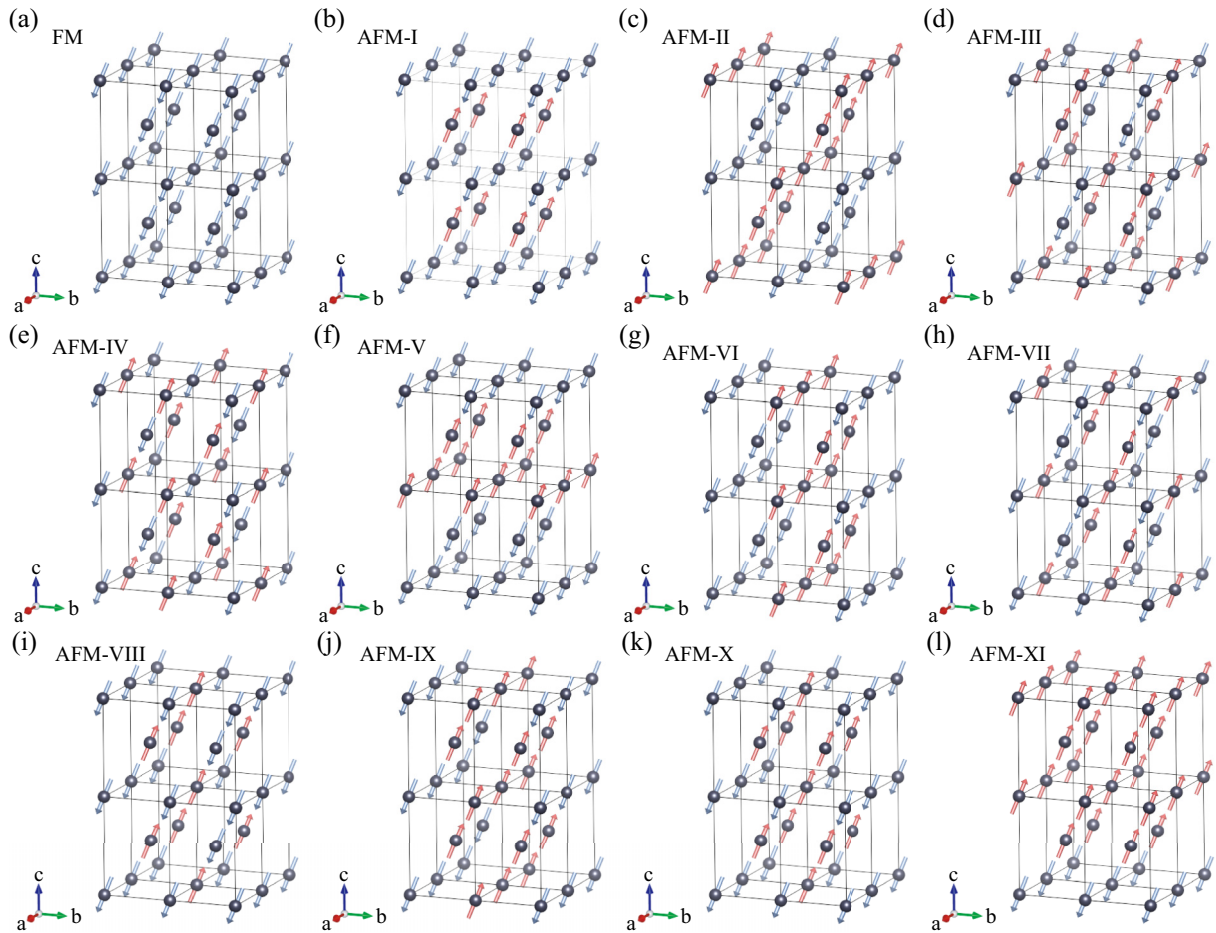


FIG. 6. Twelve different representative spin configurations of SNWO, including the (a) ferromagnetic (FM) and (b)–(l) antiferromagnetic (AFM)–I–XI structures.

and $\varphi = 133^\circ$, marked by the red star in Fig. 5(a)], with a tiny difference of only 6.9° .

As mentioned above in Sec. III C, a previous DFT study proposed the AFM-II configuration with the moments aligned along the c axis as the possible magnetic ground state [26]. However, it is clear from Fig. 3(e) that the experimentally determined direction of \vec{m}_{exp} deviates from the c axis, with a canting angle of 29.2° , which is supported by our detailed MAE calculation, as shown in Fig. 5(a). To address the discrepancy between this paper and Ref. [26], we have checked the θ dependencies of the calculated MAE for fixed φ (or the out-of-plane MAE). As shown in Fig. 5(c), if ignoring the in-plane anisotropy and fixing the moment in the xz plane ($\varphi = 0$), the MAE curve will reach a local minimum at $\theta = 90^\circ$, corresponding to the spin alignment along the c axis, which is consistent with the result in Ref. [26]. However, since the in-plane MAE shows periodic modulations [see Fig. 5(b)], the effect of φ must be considered, and the real minimum of the MAE must be sought globally throughout the 2D mapping. By fixing φ as the experimentally determined value of 133° , the MAE curve reaches an even lower minimum at $\theta = 50.4^\circ$ [see Fig. 5(c)], close to $\theta = 60.8^\circ$ found experimentally, therefore supporting our model with the Ni^{2+} moments canting off the c axis. In addition, we note that the out-of-plane modulation of the MAE

shown in Fig. 5(c) is much stronger than that of the in-plane MAE.

Furthermore, to verify the stability of the experimentally determined AFM-II structure against other possibilities, the free energies of SNWO with 12 different representative spin configurations of the Ni^{2+} moments, as shown in Figs. 6(a)–6(l), are calculated. The energies of these configurations with the moments all aligned along the c axis have already been calculated by the GGA + U method in Ref. [26]. Here, we have further incorporated the effect of SOC and set the initial moment direction the same as \vec{m}_{exp} , the experimentally determined one. Table III lists the calculation results of the relative energies with respect to the ground state. It turns out that the lowest energy is indeed achieved for the AFM-II configuration, as shown in Fig. 6(c), consistent with the experimentally determined magnetic structure, further corroborating the validity of our magnetic structure model.

As mentioned in Sec. I, direct exchange couplings between the Ni^{2+} ions are negligible because of the large distance between them, and the NN and NNN superexchange couplings occurring via 90° Ni-O(W)-O-Ni and 180° Ni-O-W-O-Ni paths, respectively, must be responsible for the magnetic ordering of the Ni^{2+} moments. Based on the calculated energies of the 12 spin configurations given in Table III, we have estimated the strengths of the superexchange couplings in

TABLE III. Relative energies (in units of meV) of 12 different spin configurations for SNWO, as shown in Fig. 6, calculated using GGA+SOC+ U .

Spin configuration	Energy (meV)
FM	14.57
AFM-I	13.61
AFM-II	0.00
AFM-III	8.66
AFM-IV	13.57
AFM-V	9.32
AFM-VI	4.78
AFM-VII	8.89
AFM-VIII	7.75
AFM-IX	6.77
AFM-X	11.33
AFM-XI	11.49

SNWO, as marked in the inset of Fig. 4, using a mapping method like that used in Ref. [26]. As a result, the in-plane superexchange coupling constants are estimated to be $J_1 \sim -0.17$ meV and $J_2 \sim -2.00$ meV, while the out-plane coupling constants are $J_{1c} \sim -0.16$ meV and $J_{2c} \sim -2.46$ meV.

By mean-field approximation, the Curie-Weiss temperature can be estimated:

$$\theta_{\text{MF}} = \frac{S(S+1)}{3k_B} (4J_1 + 4J_2 + 8J_{1c} + 2J_{2c}) = -115 \text{ K},$$

based on the superexchange coupling constants estimated by our DFT calculations. This value of θ_{MF} is close to $\theta = -92.8(3)$ K extracted from the Curie-Weiss fitting as presented in Sec. III B, further validating the correctness of the magnitude of our estimated coupling constants. Furthermore, the magnitudes of the coupling constants estimated here also agree well with those calculated in Ref. [26] and determined from inelastic neutron scattering in Ref. [25], indicating the dominant role of the NNN couplings J_2 and J_{2c} in the spin Hamiltonian of SNWO, which is favorable for the antiparallel couplings between the Ni^{2+} spins along the (001) and (110) directions and the stabilization of a type-II AFM structure.

Combining the results of our neutron diffraction measurements and DFT calculations, we can reach a conclusion that SNWO is a type-II antiferromagnet with a prominent differ-

ence in the MAE. Considering the negligible SOC due to the significant quenching of the Ni^{2+} orbital moment, this strong magnetic anisotropy is likely to arise from the single-ion anisotropy associated with the $S = 1$ Ni^{2+} ions [44–46]. Another scenario responsible for the strong magnetic anisotropy might be some underlying magnetoelastic coupling [47–49]. Further temperature-dependent XRD and NPD studies will be crucial to figure out the delicate structural change of SNWO across T_N , including the lattice constants, the atomic displacement parameters, the NiO_6 octahedral rotation or distortion, and so on.

IV. CONCLUSIONS

In summary, we have conducted comprehensive investigations on the magnetic ordering in the DP compound Sr_2NiWO_6 , combining macroscopic magnetic characterizations, NPD measurements, and DFT calculations. Below $T_N = 56$ K, SNWO is revealed to order magnetically in a type-II AFM structure with $k = (0.5, 0, 0.5)$. Due to a significant quenching of the orbital moment, the low-temperature magnetic properties of the Ni^{2+} ions can be well described by $S = 1$ in the spin-only case, and the ordered moment at 1.5 K is determined to be $1.9(2)\mu_B$. In the ground state, the Ni^{2+} moments in SNWO are estimated to cant off the c axis by 29.2° , which is well supported by the DFT calculations. In addition, the strengths of the in-plane and out-of-plane NNN superexchange couplings J_2 and J_{2c} deduced from the DFT results are found to be dominant in the spin Hamiltonian of SNWO, which accounts for the stabilization of the type-II AFM structure as its magnetic ground state.

ACKNOWLEDGMENTS

This paper is partly based on experiments performed at the Swiss Spallation Neutron Source SINQ, Paul Scherrer Institute, Villigen, Switzerland. The authors acknowledge the computational support from HPC of the Beihang University. The work at Beihang University is financially supported by the National Natural Science Foundation of China (Grant No. 12074023) and the Fundamental Research Funds for the Central Universities in China. The work at the University of Macau was supported by the Science and Technology Development Fund, Macao SAR (Files No. 0051/2019/AFJ, No. 0090/2021/A2, and No. 0049/2021/AGJ) and the University of Macau (No. MYRG2020-00278-IAPME and No. EF030/IAPME-LHF/2021/GDSTIC).

- [1] A. R. Chakhmouradian and P. M. Woodward, Celebrating 175 years of perovskite research: A tribute to Roger H. Mitchell, *Phys. Chem. Miner.* **41**, 387 (2014).
- [2] J. P. Attfield, P. Lightfoot, and R. E. Morris, *Perovskites*, *Dalton Trans.* **44**, 10541 (2015).
- [3] A. Fakharuddin, M. K. Gangishetty, M. Abdi-Jalebi, S.-H. Chin, A. bin Mohd Yusoff, D. N. Congreve, W. Tress, F. Deschler, M. Vasilopoulou, H. J. Bolink *et al.*, Perovskite light-emitting diodes, *Nat. Electron.* **5**, 203 (2022).
- [4] A. Privitera, M. Righetto, F. Cacialli, and M. K. Riede, Perspectives of organic and perovskite-based spintronics, *Adv. Opt. Mater.* **9**, 2170053 (2021).
- [5] Y.-H. Huang, R. I. Dass, Z.-L. Xing, and J. B. Goodenough, Double perovskites as anode materials for solid-oxide fuel cells, *Science* **312**, 254 (2006).
- [6] M. A. Green, A. Ho-Baillie, and H. J. Snaith, The emergence of perovskite solar cells, *Nat. Photon.* **8**, 506 (2014).
- [7] S. Vasala and M. Karppinen, $A_2B'B''O_6$ perovskites: A review, *Prog. Solid State Chem.* **43**, 1 (2015).
- [8] A. Hossain, P. Bandyopadhyay, and S. Roy, An overview of double perovskites $A_2B'B''O_6$ with small ions at A site: Synthesis, structure and magnetic properties, *J. Alloys Compd.* **740**, 414 (2018).

- [9] K.-I. Kobayashi, T. Kimura, H. Sawada, K. Terakura, and Y. Tokura, Room-temperature magnetoresistance in an oxide material with an ordered double-perovskite structure, *Nature* **395**, 677 (1998).
- [10] Y. Tomioka, T. Okuda, Y. Okimoto, R. Kumai, K.-I. Kobayashi, and Y. Tokura, Magnetic and electronic properties of a single crystal of ordered double perovskite $\text{Sr}_2\text{FeMoO}_6$, *Phys. Rev. B* **61**, 422 (2000).
- [11] K.-I. Kobayashi, T. Kimura, Y. Tomioka, H. Sawada, K. Terakura, and Y. Tokura, Intergrain tunneling magnetoresistance in polycrystals of the ordered double perovskite $\text{Sr}_2\text{FeReO}_6$, *Phys. Rev. B* **59**, 11159 (1999).
- [12] A. Kolchinskaya, P. Komissinskiy, M. B. Yazdi, M. Vafae, D. Mikhailova, N. Narayanan, H. Ehrenberg, F. Wilhelm, A. Rogalev, and L. Alff, Magnetism and spin-orbit coupling in Ir-based double perovskites $\text{La}_{2-x}\text{Sr}_x\text{CoIrO}_6$, *Phys. Rev. B* **85**, 224422 (2012).
- [13] M.-C. Lee, S. Lee, C. J. Won, K. D. Lee, N. Hur, J.-L. Chen, D.-Y. Cho, and T. W. Noh, Hybridized orbital states in spin-orbit coupled $3d-5d$ double perovskites studied by x-ray absorption spectroscopy, *Phys. Rev. B* **97**, 125123 (2018).
- [14] W. Jin, S. H. Chun, J. Kim, D. Casa, J. P. C. Ruff, C. J. Won, K. D. Lee, N. Hur, and Y.-J. Kim, Magnetic excitations in the double-perovskite iridates La_2MIrO_6 ($M = \text{Co}, \text{Ni}, \text{and Zn}$) mediated by $3d-5d$ hybridization, *Phys. Rev. B* **105**, 054419 (2022).
- [15] P. Battle and C. Jones, The crystal and magnetic structures of $\text{Sr}_2\text{LuRuO}_6$, Ba_2YRuO_6 , and $\text{Ba}_2\text{LuRuO}_6$, *J. Solid State Chem.* **78**, 108 (1989).
- [16] E. Rodríguez, M. L. López, J. Campo, M. L. Veiga, and C. Pico, Crystal and magnetic structure of the perovskites La_2MTiO_6 ($M = \text{Co}, \text{Ni}$), *J. Mater. Chem.* **12**, 2798 (2002).
- [17] S. J. Makowski, J. A. Rodgers, P. F. Henry, J. P. Attfield, and J.-W. G. Bos, Coupled spin ordering in the $\text{Ln}_2\text{LiRuO}_6$ double perovskites, *Chem. Mater.* **21**, 264 (2009).
- [18] T. Koga, N. Kurita, M. Avdeev, S. Danilkin, T. J. Sato, and H. Tanaka, Magnetic structure of the $S = \frac{1}{2}$ quasi-two-dimensional square-lattice Heisenberg antiferromagnet $\text{Sr}_2\text{CuTeO}_6$, *Phys. Rev. B* **93**, 054426 (2016).
- [19] S. Vasala, M. Avdeev, S. Danilkin, O. Chmaissem, and M. Karppinen, Magnetic structure of Sr_2CuWO_6 , *J. Phys.: Condens. Matter* **26**, 496001 (2014).
- [20] S. Nomura and T. Nakagawa, Magnetic properties and optical and paramagnetic spectra of divalent nickel in $\text{Sr}_2(\text{NiW})\text{O}_6$, *J. Phys. Soc. Jpn.* **21**, 1679 (1966).
- [21] D. Iwanaga, Y. Inaguma, and M. Itoh, Structure and magnetic properties of Sr_2NiAO_6 ($A = \text{W}, \text{Te}$), *Mater. Res. Bull.* **35**, 449 (2000).
- [22] C. Blum, A. Holcombe, M. Gellesch, M. Sturza, S. Rodan, R. Morrow, A. Maljuk, P. Woodward, P. Morris, A. Wolter *et al.*, Flux growth and characterization of Sr_2NiWO_6 single crystals, *J. Cryst. Growth* **421**, 39 (2015).
- [23] M. Gateshki, J. Igartua, and E. Hernandez-Bocanegra, X-ray powder diffraction results for the phase transitions in Sr_2MWO_6 ($M = \text{Ni}, \text{Zn}, \text{Co}, \text{Cu}$) double perovskite oxides, *J. Phys.: Condens. Matter* **15**, 6199 (2003).
- [24] Q. Zhou, B. J. Kennedy, C. J. Howard, M. M. Elcombe, and A. J. Studer, Structural phase transitions in $\text{A}_{2-x}\text{Sr}_x\text{NiWO}_6$ ($A = \text{Ca or Ba}, 0 \leq x \leq 2$) double perovskites, *Chem. Mater.* **17**, 5357 (2005).
- [25] Y. Todate, Exchange interactions in antiferromagnetic complex perovskites, *J. Phys. Chem. Solids* **60**, 1173 (1999).
- [26] N. Rezaei, T. Hashemifar, M. Alaei, F. Shahbazi, S. J. Hashemifar, and H. Akbarzadeh, *Ab initio* investigation of magnetic ordering in the double perovskite Sr_2NiWO_6 , *Phys. Rev. B* **99**, 104411 (2019).
- [27] D. Cox, G. Shirane, and B. Frazer, Neutron-diffraction study of antiferromagnetic Ba_2CoWO_6 and Ba_2NiWO_6 , *J. Appl. Phys.* **38**, 1459 (1967).
- [28] P. Fischer, G. Frey, M. Koch, M. Könecke, V. Pomjakushin, J. Schefer, R. Thut, N. Schlumpf, R. Bürge, U. Greuter *et al.*, High-resolution powder diffractometer HRPT for thermal neutrons at SINQ, *Phys. B: Condens. Matter* **276-278**, 146 (2000).
- [29] J. Rodríguez-Carvajal, Recent advances in magnetic structure determination by neutron powder diffraction, *Phys. B: Condens. Matter* **192**, 55 (1993).
- [30] J. P. Perdew, K. Burke, and M. Ernzerhof, Generalized Gradient Approximation Made Simple, *Phys. Rev. Lett.* **77**, 3865 (1996).
- [31] G. Kresse and J. Furthmüller, Efficient iterative schemes for *ab initio* total-energy calculations using a plane-wave basis set, *Phys. Rev. B* **54**, 11169 (1996).
- [32] G. Kresse and D. Joubert, From ultrasoft pseudopotentials to the projector augmented-wave method, *Phys. Rev. B* **59**, 1758 (1999).
- [33] V. I. Anisimov, J. Zaanen, and O. K. Andersen, Band theory and Mott insulators: Hubbard U instead of Stoner I , *Phys. Rev. B* **44**, 943 (1991).
- [34] O. Bengone, M. Alouani, P. Blöchl, and J. Hugel, Implementation of the projector augmented-wave LDA+U method: Application to the electronic structure of NiO, *Phys. Rev. B* **62**, 16392 (2000).
- [35] L. Xu, C. Qin, Y. Wan, H. Xie, Y. Huang, L. Qin, and H. J. Seo, Sol-gel preparation, band structure, and photochemical activities of double perovskite A_2NiWO_6 ($A = \text{Ca}, \text{Sr}$) nanorods, *J. Taiwan Inst. Chem. Eng.* **71**, 433 (2017).
- [36] A. M. Glazer, The classification of tilted octahedra in perovskites, *Acta Cryst. B* **28**, 3384 (1972).
- [37] K. Somesh, Y. Furukawa, G. Simutis, F. Bert, M. Prinz-Zwick, N. Büttgen, A. Zorko, A. A. Tsirlin, P. Mendels, and R. Nath, Universal fluctuating regime in triangular chromate antiferromagnets, *Phys. Rev. B* **104**, 104422 (2021).
- [38] K. Ranjith, K. Brinda, U. Arjun, N. Hegde, and R. Nath, Double phase transition in the triangular antiferromagnet $\text{Ba}_3\text{CoTa}_2\text{O}_9$, *J. Phys.: Condens. Matter* **29**, 115804 (2017).
- [39] N. Kini, E. Kaul, and C. Geibel, $\text{Zn}_2\text{VO}(\text{PO}_4)_2$: An $S = \frac{1}{2}$ Heisenberg antiferromagnetic square lattice system, *J. Phys.: Condens. Matter* **18**, 1303 (2006).
- [40] M. Reynaud, J. Rodríguez-Carvajal, J.-N. Chotard, J.-M. Tarascon, and G. Rousse, Magnetic structure and properties of orthorhombic $\text{Li}_2\text{Ni}(\text{SO}_4)_2$: A possible magnetoelectric material, *Phys. Rev. B* **89**, 104419 (2014).
- [41] K. M. Ranjith, R. Nath, M. Majumder, D. Kasinathan, M. Skoulatos, L. Keller, Y. Skourski, M. Baenitz, and A. A. Tsirlin, Commensurate and incommensurate magnetic order in spin-1 chains stacked on the triangular lattice in $\text{Li}_2\text{NiW}_2\text{O}_8$, *Phys. Rev. B* **94**, 014415 (2016).
- [42] C. Su, X.-T. Zeng, Y. Li, N. Ma, Z. Lin, C. Zhang, C.-W. Wang, Z. Chen, X. Lu, W. Li *et al.*, Zigzag magnetic order in a novel tellurate compound $\text{Na}_{4-s}\text{NiTeO}_6$ with $S = 1$ chains, *Sci. China Phys. Mech. Astron.* **65**, 297511 (2022).

- [43] A. Azad, S.-G. Eriksson, A. Møllergård, S. Ivanov, J. Eriksen, and H. Rundlöf, A study on the nuclear and magnetic structure of the double perovskites $A_2\text{FeWO}_6$ ($A = \text{Sr}, \text{Ba}$) by neutron powder diffraction and reverse monte carlo modeling, *Mater. Res. Bull.* **37**, 1797 (2002).
- [44] A. P. Ramirez, S.-W. Cheong, and M. L. Kaplan, Specific Heat of Defects in Haldane Systems Y_2BaNiO_5 and NENP: Absence of free Spin- $\frac{1}{2}$ Excitations, *Phys. Rev. Lett.* **72**, 3108 (1994).
- [45] S. A. Zvyagin, J. Wosnitzer, C. D. Batista, M. Tsukamoto, N. Kawashima, J. Krzystek, V. S. Zapf, M. Jaime, N. F. Oliveira, and A. Paduan-Filho, Magnetic Excitations in the Spin-1 Anisotropic Heisenberg Antiferromagnetic Chain System $\text{NiCl}_2\cdot 4\text{SC}(\text{NH}_2)_2$, *Phys. Rev. Lett.* **98**, 047205 (2007).
- [46] S. P. M. Curley, R. Scatena, R. C. Williams, P. A. Goddard, P. Macchi, T. J. Hicken, T. Lancaster, F. Xiao, S. J. Blundell, V. Zapf *et al.*, Magnetic ground state of the one-dimensional ferromagnetic chain compounds $M(\text{NCS})_2(\text{thiourea})_2$ ($M = \text{Ni}, \text{Co}$), *Phys. Rev. Mater.* **5**, 034401 (2021).
- [47] K. Dutta, Magnetoelastic coupling and critical behavior of some strongly correlated magnetic systems, *J. Phys.: Condens. Matter* **35**, 083001 (2021).
- [48] S. Lee, M.-C. Lee, Y. Ishikawa, P. Miao, S. Torii, C. J. Won, K. D. Lee, N. Hur, D.-Y. Cho, and T. Kamiyama, Magnetoelastic octahedral breathing mode in the ferrimagnetic $\text{La}_2\text{CoIrO}_6$ double perovskite, *Phys. Rev. B* **98**, 104409 (2018).
- [49] D. Serrate, J. M. De Teresa, P. A. Algarabel, C. Marquina, J. Blasco, M. R. Ibarra, and J. Galibert, Magnetoelastic coupling in $\text{Sr}_2(\text{Fe}_{1-x}\text{Cr}_x)\text{ReO}_6$ double perovskites, *J. Phys.: Condens. Matter* **19**, 436226 (2007).